# Electronic Supplementary Information

## High Temperature Driven Inter-valley Carrier Transfer and Significant Fluorescence Enhancement in Multilayer WS$_2$

Heyu Chen,[1] Yuanzheng Li,[1] Weizhen Liu,[1,3,*] Haiyang Xu,[1,*] Guochun Yang,[1] Jia Shi,[2] Qiushi Feng,[1] Tong Yu,[1] Xinfeng Liu[2] and Yichun Liu[1]

[1]Centre for Advanced Optoelectronic Functional Materials Research and Key Laboratory of UV-Emitting Materials and Technology (Northeast Normal University), Ministry of Education, Changchun 130024, China

[2]Division of Nanophotonics, CAS Key Laboratory of Standardization and Measurement for Nanotechnology, CAS Center for Excellence in Nanoscience, National Center for Nanoscience and Technology, Beijing 100190, China

[3]National Demonstration Center for Experimental Physics Education (Northeast Normal University), Changchun 130024, China

*Email: wzliu@nenu.edu.cn and hyxu@nenu.edu.cn

# Note 1: Details for Carrier Population Ratio Calculations

At room temperature, most photo-generated electrons and holes in ML-WS$_2$ are situated at the $\Lambda$ valley (CBM) and $\Gamma$ hill (VBM), respectively. However, as the temperature rises, the kinetic energy of excited-state carriers would be increased due to the stronger thermal motion, and electrons/holes will repopulate among different energy valleys/hills following the Boltzmann-distribution-law. Here, we define the numbers of electrons occupying the K and $\Lambda$ valley as $N_1$ and $N_2$, respectively. Similarly, hole numbers at the K and $\Gamma$ hill can be respectively set as $P_1$ and $P_2$. Then, the electron number ratio between the K valley and $\Lambda$ valley and the hole number ratio between the K hill and $\Gamma$ hill can be obtained using the following expressions:[1-3]

$$\frac{N_1}{N_2} = R_e \times \exp\left(-\frac{\Delta E_{\Lambda-K}}{kT_e}\right) \qquad (1)$$

$$\frac{P_1}{P_2} = R_h \times \exp\left(-\frac{\Delta E_{\Gamma-K}}{kT_h}\right) \qquad (2)$$

From the above two equations, the population ratios of K valley electrons ($N_1/(N_1+N_2)$) and K hill holes ($P_1/(P_1+P_2)$) and those of $\Lambda$ valley electrons ($N_2/(N_1+N_2)$) and $\Gamma$ hill holes ($P_2/(P_1+P_2)$) could be respectively written as follows:

$$\frac{N_1}{N_1+N_2} = \frac{R_e \times exp(-\frac{\Delta E_{\Lambda-K}}{kT_e})}{1 + R_e \times exp(-\frac{\Delta E_{\Lambda-K}}{kT_e})} \qquad (3)$$

$$\frac{N_2}{N_1+N_2} = \frac{1}{1 + R_e \times exp(-\frac{\Delta E_{\Lambda-K}}{kT_e})} \qquad (4)$$

$$\frac{P_1}{P_1+P_2} = \frac{R_h \times exp(-\frac{\Delta E_{\Gamma-K}}{kT_h})}{1 + R_h \times exp(-\frac{\Delta E_{\Gamma-K}}{kT_h})} \qquad (5)$$

$$\frac{P_2}{P_1 + P_2} = \frac{1}{1 + R_h \times exp(-\frac{\Delta E_{\Gamma-K}}{kT_h})} \quad (6)$$

In these equations, $\Delta E_{\Lambda-K}$ is the conduction band energy difference between $\Lambda$ valley and K valley and $\Delta E_{\Gamma-K}$ is the valence band energy difference between $\Gamma$ hill and K hill; k is the Boltzmann constant; $T_e$ and $T_h$ are the effective lattice temperatures for electrons and holes. For simplicity, $T_e$ and $T_h$ are supposed to be the same as environment temperatures. $R_e$ and $R_h$ are the density-of-state ratios for electrons in K valley and $\Lambda$ valley and for holes at K hill and $\Gamma$ hill, respectively.

The parameters $R_e$, $R_h$ and $\Delta E_{\Lambda-K}$, $\Delta E_{\Gamma-K}$ can be obtained from other literatures and our DFT calculations, respectively. They are listed in the **Tab.S1** below:

|  | $R_e$ | $R_h$ | $\Delta E_{\Lambda-K}$ | $\Delta E_{\Gamma-K}$ |
|---|---|---|---|---|
| WS$_2$ | 0.77 | 5.14 | 230 meV | 40 meV |

**Tab.S1** The parameters employed for the calculations.[4-6]

By taking these parameters into the equations above, the temperature-dependent carrier population ratios among different energy valleys and hills can be obtained, as shown in **Fig. 1**(c) and (d) in the main text.

## Note 2: Comparison of Radiative Recombination Probability at the K and Λ/Γ point

According to the calculations in **Note 1**, the population ratio of photo-carriers at the K point (including K-valley and K-hill) is improved ~1000-fold when the environmental temperature is increased from 300 to 760 K. Although a tremendous increase of K-point carrier popoulation is achieved, the actual carrier population ratios at the K valley for electron (~0.02) and K hill for hole (~0.45) are still smaller than those at the Λ valley for electron (~0.98) and Γ hill for hole (~0.55). In addition to the carrier popoulation ratio, radiative recombination probability is another important factor that affects the practical fluorecence emisison intensity of different optical transitions. Herein, a comparison between the radiative recombination probability of different transition processes is made. We assume the radiative recombination probability at the K valley and K hill as $P_{Ke}$ and $P_{Kh}$ for electrons and holes, respectively. Simillarly, the radiative recombination probability of Λ valley electrons and Γ hill holes are set as $P_{Λe}$ and $P_{Γh}$, respectively. The integrated intensity ratio of the K→K direct emission to Λ→Γ indirect emission ($I_{K→K}/I_{Λ→Γ}$) can be approximately expressed as:[15]

$$\frac{I_{K→K}}{I_{Λ→Γ}} = \frac{N_1}{N_2} \times \frac{P_{Ke}}{P_{Λe}} \qquad (7)$$

$$\frac{I_{K→K}}{I_{Λ→Γ}} = \frac{P_1}{P_2} \times \frac{P_{Kh}}{P_{Γh}} \qquad (8)$$

where $N_1/N_2$ is the ratio of electron number at the K valley and Λ valley, $P_1/P_2$ is the number ratio of hole at the K hill and Γ hill (see **Note 1** for detailed calculation). Take the value of $N_1/N_2$, $P_1/P_2$ and $I_{K→K}/I_{Λ→Γ}$ at 760 K into equation (7) and (8), the ratio of radiative recombination probability can be obtained as follows:

$$\frac{P_{Ke}}{P_{Λe}} = 245$$

$$\frac{P_{Kh}}{P_{Γh}} = 6$$

The results demomstrate that the $P_K$ (including $P_{Ke}$ and $P_{Kh}$) of K-point-related direct transition is generally one to two orders of magnitude higher than the $P_{A/\Gamma}$ (including $P_{Ae}$ and $P_{\Gamma h}$) of $\Lambda/\Gamma$-point-related indirect transitions. Thus, the PL intensity of the K→K direct emission is much stronger than that of the $\Lambda$→$\Gamma$ indirect emission at elevated temepratures, even though most carriers are still located at the $\Lambda/\Gamma$ points.

# Note 3: Data Fitting for Time-Resolved PL Spectra of ML-WS$_2$ at High Temperatures

In the main text, the time-resolved PL spectra of the K→K direct emission at different temperatures are plotted in **Fig. 5**. Here, the transient-state PL spectra at six different temperatures could be well fitted by an exponential attenuation function: $I = A\exp(-t/\tau) + I_0$, where I and $I_0$ are the PL intensity, and $\tau$ is the corresponding fluorescence lifetime. The detailed fitting results are shown in the following **Tab. S2**.

| Temperature | 300K | 360K | 440K | 520K | 600K | 680K |
|---|---|---|---|---|---|---|
| $I_0$ | 22.27 | 21.65 | 20.46 | 20.32 | 26.76 | 25.46 |
| $\tau$ | 80$\pm$1 | 82$\pm$0.6 | 85$\pm$0.8 | 96$\pm$1.6 | 103$\pm$1.7 | 120$\pm$2 |

**Tab. S2** Fitting parameters of the time-resolved PL spectra shown in **Fig.5**

# Note 4: Discussion about the Calculation of Electronic Band Structure

It is noteworthy that heating up not only leads to the lattice expansion, but also causes the bandgap structure modification via strengthened electron-phonon interactions.[7-10] The former has been considered in our first-principles calculations of the multilayer $WS_2$ bandgap structure, whereas the latter is not involved in the calculation process. This is because involving thermo-induced electron-phonon interaction in the DFT simulations will make the whole calculation process extremely complex and difficult, which may not even give out a direct calculation result. Thus, the vast majority of reported bandgap calculations using DFT method are carried out at absolute 0 K, and do not consider the actual environmental temperature.[11-14] So, it is a pity that we fail to take into account the thermo-induced electron-phonon interaction during the DFT simulations, which is beyond the scope of our calculation ability.

Although the accurate calculation of bandgap structure variation is difficult, Zhao *et al.* theoretically evaluated the influence of electron-phonon interaction on the bandgap structure of multilayer $MoS_2$, $WS_2$ and $WSe_2$.[23] It is claimed that the electron-phonon coupling effect appears to enhance the temperature-dependent bandgap shift, which is beyond the prediction by the DFT results. A general trend is that the bandgap energy decreases with temperature above the Debye temperature ($T_D$), and keeps nearly invariable as the temperature is far below the $T_D$.

In the current case, the K valley moves downward and K hill moves upward, while $\Lambda$ valley shifts up and $\Gamma$ hill shifts down when the environment temperature is elevated.[17, 23] Such a scenario will reduce the $\Delta E_{\Lambda\text{-K}}$ in conduction band and $\Delta E_{\Gamma\text{-K}}$ in valence band. That is, the potential barrier for carrier transfer decreases, which is beneficial for the inter-valley transfer of photocarriers. However, the precise positions of K valley/hill, $\Lambda$ valley and $\Gamma$ hill with increasing temperature cannot be obtained at the current stage. In addition, the proposed inter-valley transfer model is just an initial prototype, which needs to be further optimized. These issues will be our future research topic and deserve more in-depth investigation by improving the calculation
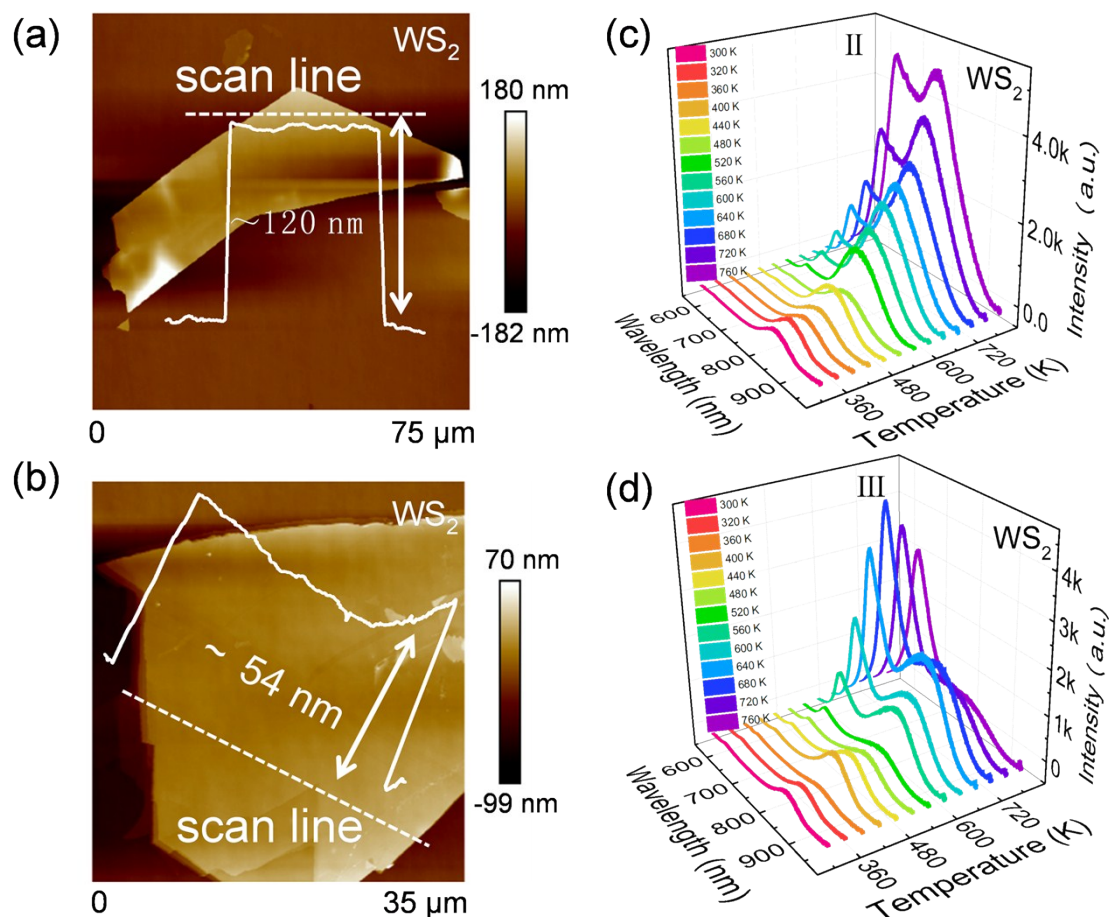
method, relevant structure model and parameter setting.

**Fig.S1** (a) and (b) Typical AFM images of other two ML-WS$_2$ samples with different thickness of 120 nm (~150-layer) and 54 nm (~68-layer). (c) and (d) The TD-PL spectra of these two ML-samples meassured in argon atmosphere; the test temperature ranges from 300 to 760 K.

To verify the reproducibility and reliability of the high-temperature-induced PL enhancement phenomenon, TD-PL measurements are performed on another two ML-WS$_2$ flakes with different thickness in argon atmosphere. As is shown, similar high-temperature induced fluorescence emission enhancements could be observed as well. A decrease in the PL intensity is observed for the 68-layer WS$_2$ sample after temperature higher than 680 K, which may be caused by the thermal quenching effect. These results indicate that the observed luminescence enhancements of ML-WS$_2$ at elevated temperatures are reliable and reproducible.
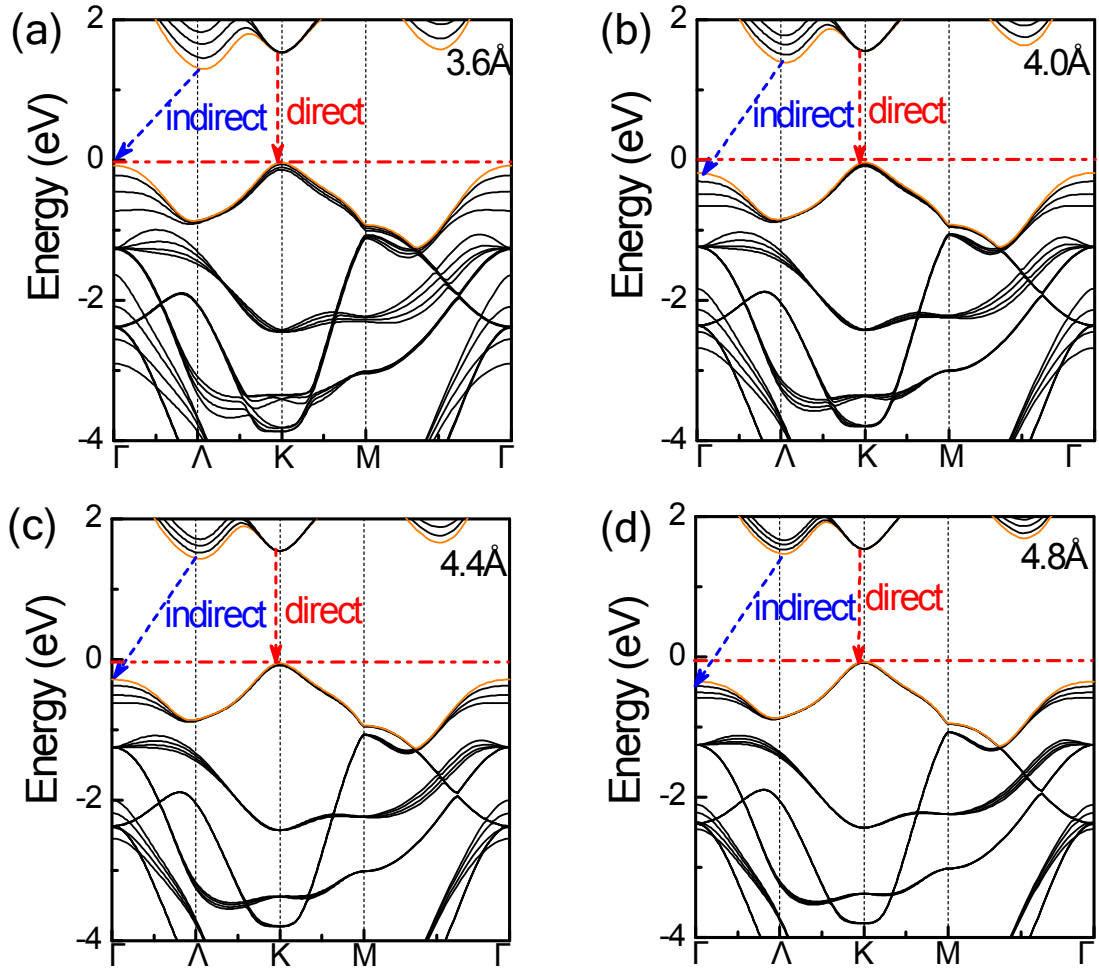
**Fig.S2** (a) to (d) show the DFT calculated energy band structures of 4-layer $WS_2$ with c-axis interlayer distance of 3.6 Å, 4.0 Å, 4.4 Å and 4.8 Å respectively. These figures present the evolution trend of ML-$WS_2$ band strcuture from indirect to direct bandgap with the increasing c-axis interlayer distance.
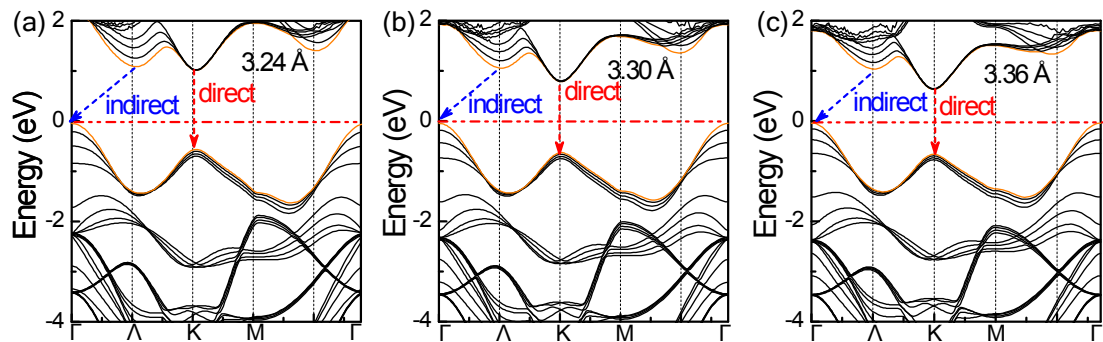


**Fig.S3** (a) (b) and (c) show the energy band structures of 4-layer $WS_2$ with a-axis lattice constants of 3.24 Å,3.3 Å and 3.36 Å respectively. The variation trend of bandgap with the increasing a-axis lattice constant can be observed in these schemes.
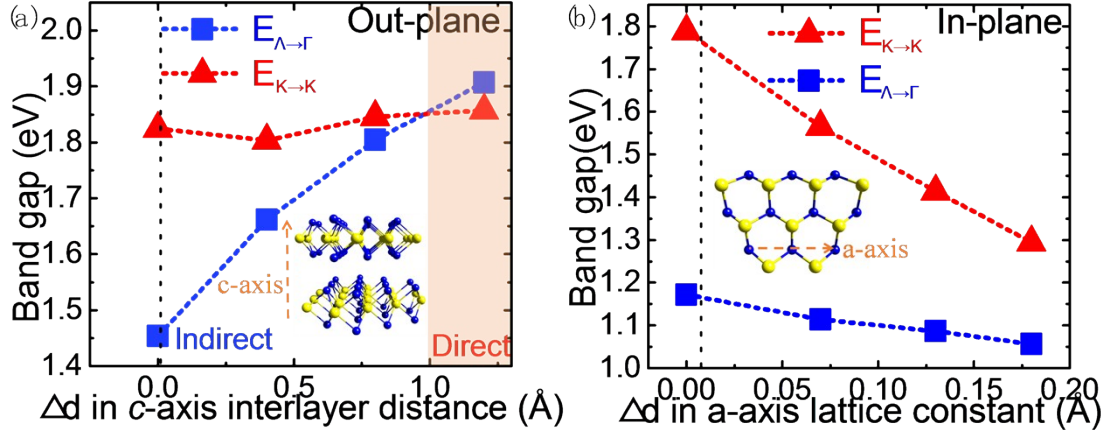
**Fig.S4** The direct ($E_{K-K}$) and indirect ($E_{\Lambda-\Gamma}$) band-gap of $WS_2$ as a function of the c-axis interlayer distance (a) and the a-axis lattice constants (b). The insets show the direction of c/a-axis in the structural schematic diagram of $WS_2$. The black vertical dashed lines plotted in (a) and (b) show the estimated increments of c-axis interlayer distance (~0.005 Å) and a-axis lattice constants (~0.009 Å) at 760 K. The increments were calculated on the basis of the thermal expansion coefficient of ML-$WS_2$.

In a previous study,[16] an interlayer decoupling process is considered as the main reason for the enhancement of direct transition emission. It is thought that if the temperature is high enough, the c-axis interlayer spacing might be greatly enlarged as a result of the lattice thermal expansion. This may turn the ML-$WS_2$ into an assembly of many isolated monolayer $WS_2$, and switch the band-gap structure of ML-$WS_2$ from indirect transition to direct transition. Thus, the fluorescence emission intensity is enhanced at high temperatures.

In order to prove that the interlayer decoupling process discussed above cannot really happen in the current experiment, a series of DFT calculations of the electronic structure have been done on the ML-$WS_2$. Herein, a 4L-$WS_2$ model is used as the geometry configuration in the calculation, because the band structure of ML-$WS_2$ is almost the same when the sample thickness is no less than four-layer.[17, 18] Geometry optimizations and electronic structure calculations were performed within the framework of density functional theory as implemented in the Vienna ab initio Simulation Package (VASP) code.[19] To accurately describe the van der waals (vdW)

interactions between neighboring interlayers,[20] a semi-empirical correction to the Kohn-Sham energy was adopted. The exchange correlation energy was described by the generalized gradient approximation (GGA) in the scheme proposed by Perdew-Burke-Ernzerhof (PBE),[21] which is broadly used due to its accuracy and economy. The ion-electron interaction was treated by the projector augmented wave (PAW) technique with $5d^46S^2$ and $3S^23P^4$ for W and S, respectively.[22] The plane-wave kinetic energy cutoff of 550 eV was used. The Brillouin zone was sampled with $13 \times 13 \times 1$ $\Gamma$ centered $k$ points grid. A vacuum spacing of 15 Å was added along the c-axis for the two-dimensional structure calculations. The optimized lattice constants in our calculations are listed in the following **Tab.S3**.

| Lattice Orientation | a-axis | b-axis | c-axis |
|---|---|---|---|
| Lattice Constant (Å) | 3.17 | 3.17 | 12.47 |

**Tab.S3** Optimized lattice constants in the current DFT calculations.

It should be noted that the cubical expansion of the ML-WS$_2$ sample will occurs in the direction of both c-axis and a-axis. Hence, the electronic structures of ML-WS$_2$ with the increasing c-axis interlayer distance (out-plane) and a-axis lattice constant (in-plane) were calculated and the results are shown in **Fig.S2** and **Fig.S3**, respectively. To clearly illustrate the band-gap evolution, the values of $E_{\Lambda\text{-}\Gamma}$ and $E_{K\text{-}K}$ as a function of c-axis and a-axis increment were extracted and shown respectively in **Fig.S4** (a) and (b). In **Fig.S4** (a), there is a crossover point from indirect to direct band-gap at $\triangle d=0.97$ Å (~30% expansion). If the $\triangle d$ in c-axis is larger than 0.97 Å, the $E_{K\text{-}K}$ will be smaller than the $E_{\Lambda\text{-}\Gamma}$ and the ML-WS$_2$ will behave as a direct band-gap semiconductor with K→K transition as the main radiative recombination pathway for photo-carriers. This phenomenon is termed as the interlayer decoupling effect of ML-WS$_2$.[16] On the other hand, as shown in **Fig.S4** (b), the values of $E_{\Lambda\text{-}\Gamma}$ and $E_{K\text{-}K}$ reduce with the increase of a-axis lattice constant and no crossover is observed at $\triangle d=0.18$ Å (~6% expansion). Our calculation results agree well with the previous studies, confirming the reliability of our DFT calculations.[23-25]

Next, let's consider the real c/a-axis distance increments induced by the thermal expansion in the current experiment. The practical increment values in c-axis interlayer distance and a-axis lattice constant of ML-WS$_2$ can be estimated by the following equations:

$$K_c = \frac{\Delta c}{c_0 \cdot \Delta T} \tag{9}$$

$$K_a = \frac{\Delta a}{a_0 \cdot \Delta T} \tag{10}$$

where $K_c$ = 3.26 × 10$^{-6}$ and $K_a$ =6.35 × 10$^{-6}$ are the linear thermal expansion coefficient along the c-axis and a-axis direction of 2H-phase WS$_2$;[26] $c_0$ = 3.2 Å and $a_0$ = 3.1 Å are the original c-axis interlayer distance and a-axis lattice constant at room temperature[27-29] $\Delta T$ = 460 K is the maximal temperature difference in the current experiments; $\Delta c$ ($\Delta a$) is the corresponding increment in c-axis interlayer distance (a-axis lattice constant). By taking these parameters into the above formulas, $\Delta c$ and $\Delta a$ are respectively estimated to be only ~0.005 and ~0.009 Å, which are illustrated by the dashed lines in the **Fig.S4** (a) and (b).

Through the simple calculations above, the actual increments of the c-axis interlayer distance and a-axis lattice constant of ML-WS$_2$ are demonstrated to be extremely small, which are much less than the estimated critical values of Δd necessary for band-gap conversion. Thus, the thermo-induced volume expansion cannot cause the interlayer decoupling effect, and cannot switch the band-gap structure of ML-WS$_2$ from the indirect to direct type in the current experiment. The decisive reason for the observed PL enhancement of ML-WS$_2$ cannot be attributed to the interlayer decoupling effect, but should be ascribed to the inter-valley carrier transfer model.
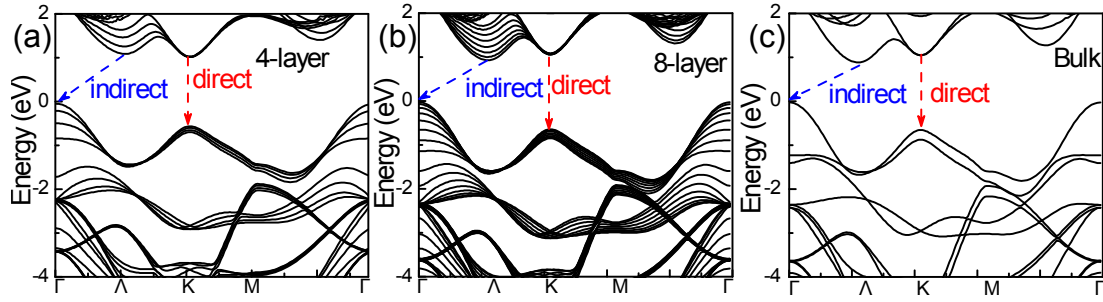
**Fig.S5** DFT calculated bandgap structure diagrams of (a) 4-layer, (b) 8-layer and (c) bulk WS$_2$ material.

The bandgap structure of multilayer WS$_2$ varies slightly with the increasing thickness. To clearly illustrate this point, bandgap structure diagrams of 4-layer, 8-layer and bulk WS$_2$ are simulated via DFT calculations and relevant results are shown in the following **Fig.S5**. As can be seen, multilayer WS$_2$ are all indirect-band-gap semiconductors in spite of their different layer numbers. However, the specific indirect-band-gap value changes slightly with the varied thickness (or layer number). For 4-layer WS$_2$, the calculated bandgap is ~1.15 eV, while it reduces to ~1.0 eV when the layer number increases to 8-layer. For the bulk WS$_2$, its indirect-band-gap value is ~0.9 eV. The shrinkage of simulated bandgap value with increasing layer number is due to the weakening of quantum confinement effect at larger thickness.[32, 33] It is noted that the simulated bandgap (~1.15 eV) is a little bit smaller than the experimentally observed value (~1.4 eV). Underestimation of material bandgap is a common phenomenon in the DFT simulations, which could be attributed to the introduction of semi-local PBE exchange-correlation function in the DFT calculation process.[34-36] Despite this, the derived variation trend of bandgap value with layer number (or thickness) is still reliable and valuable.
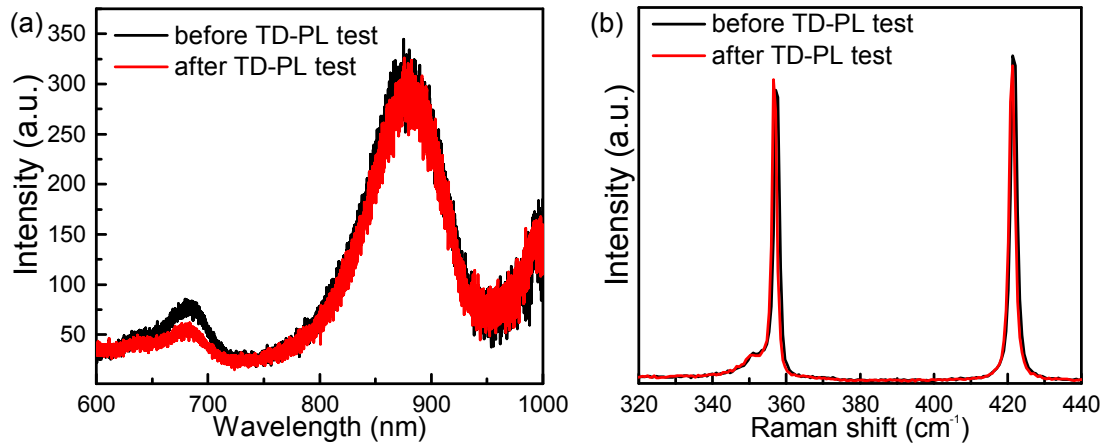
**Fig.S6** shows the room temperature in-situ PL (a) and Raman (b) spectra of the ML-WS$_2$ before (black) and after (red) the TD-PL measurements.

To detect the variations of crystalline quality, in-situ PL and Raman spectra (the measuring position is marked as a blue spot shown in **Fig.S7**) are collected (see **Fig. S6**), since the PL and Raman spectra could reflect the defect concentration, strain, lattice disorder and so forth.[4, 30] As shown in **Fig.S6** (a), insignificant changes in peak-position and FWHM occur in the PL spectra of the sample after the TD-PL test. In addition to the two original peaks, no other luminescence peaks appear in the spectrum. Moreover, in the Raman spectra of **Fig.S6** (b), no significant variations can be observed. These phenomena indicate that no distinct defects were formed during the TD-PL measurements. Thus, the observed PL variation in the main text is not induced by the formation of more defects.
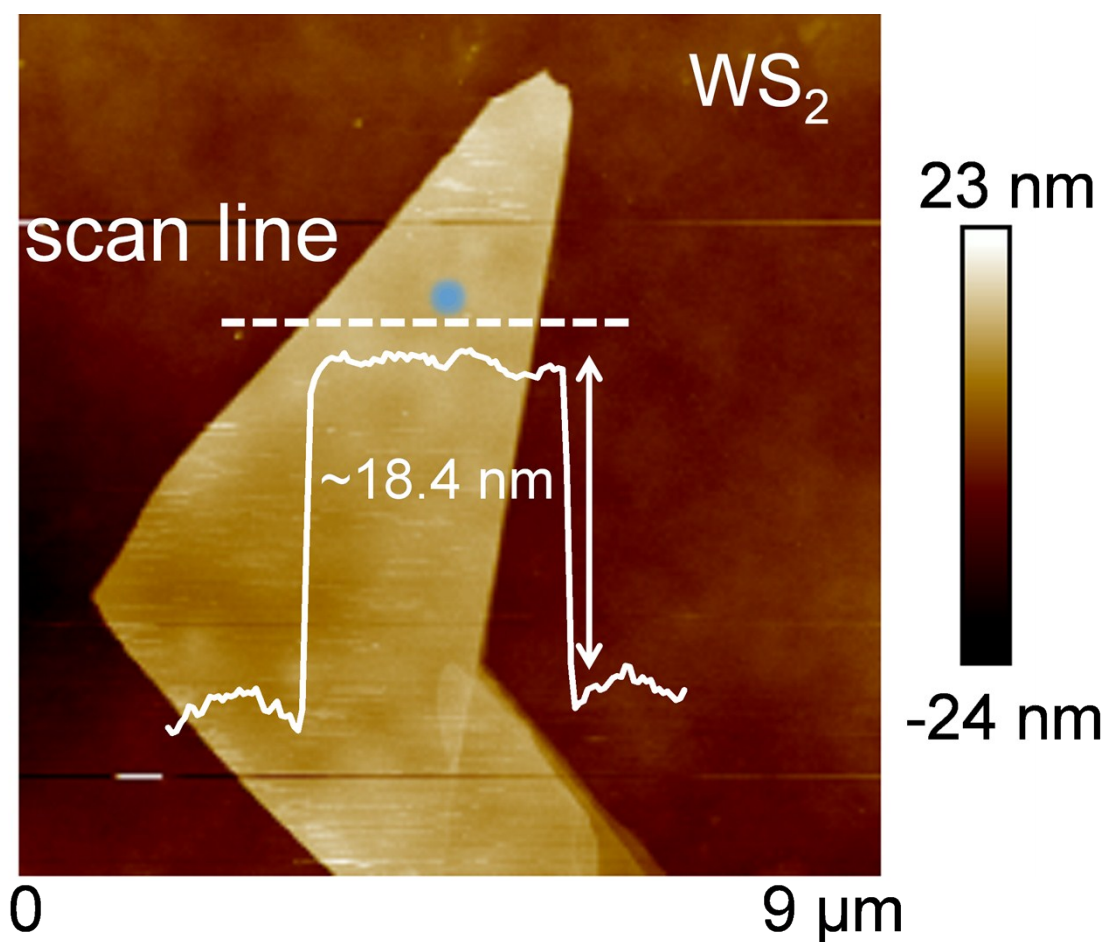
**Fig.S7** AFM image and corresponding height line-scan of the ML-WS$_2$ after the TD-PL measurement. The blue spot marked in the image is the measuring position of the in-situ Raman and PL spectra.

The AFM image and the corresponding height line-scan of the ML-WS$_2$ flake after the TD-PL test are presented in **Fig.S7**. As can be seen, no significant changes in surface topography of the sample are observed after the TD-PL measurement. In addition, the height of the sample is only changed by 0.6% after heating, indicating that the change in sample height can be ignored. WS$_2$, whose melting point is 980 K, is always used as solid lubricant coatings due to its excellent mechanical property and physical stability.[31, 37] Thus, it is concluded that the elevated temperature has ignorable influence on the quality of ML-WS$_2$ in the current research and the PL enhancement is not aroused by the sample thickness change either.
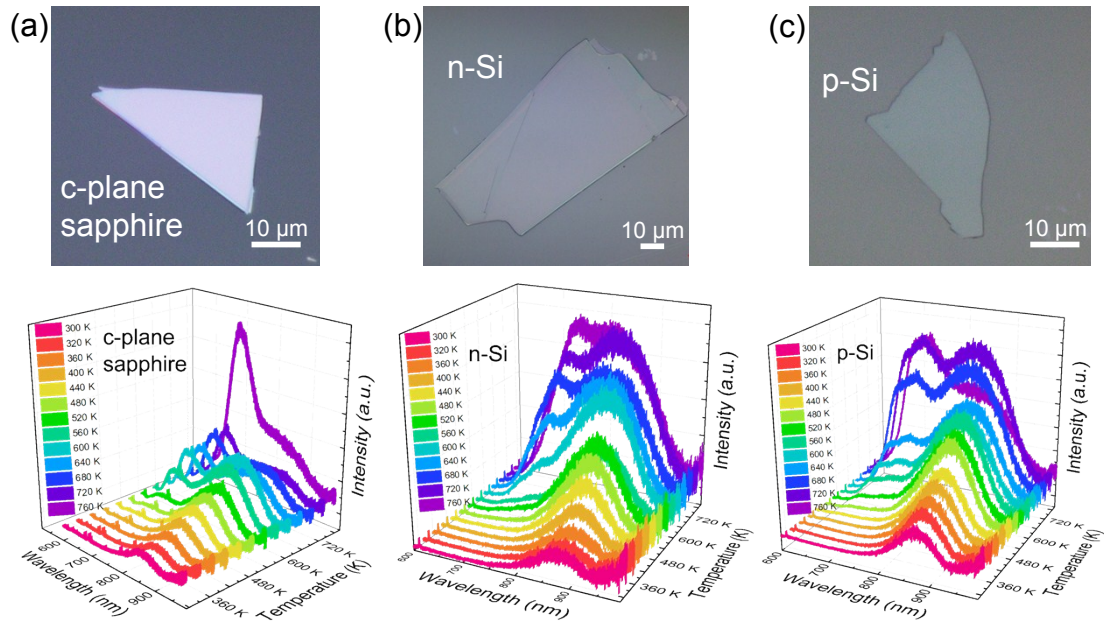
**Fig.S8** TD-PL spectra of the multilayer WS$_2$ samples on different supporting substrates: (a) c-sapphire, (b) n-Si and (c) p-Si.

The optical behavior of 2D materials may be affected by the supporting substrates. To study this effect, temperature-dependent PL spectra of the multilayer WS$_2$ samples on different supporting substrates (c-sapphire, n-Si and p-Si) are measured and corresponding results are plotted in the **Fig. S8**. As can be seen, similar fluorescence emission enhancements are observed from all these samples, although they are placed on different substrates. This fact confirms the following two points: 1) the high-temperature-induced luminescence enhancement phenomenon is credible and reproducible for the multilayer WS$_2$ on different substrates; 2) the proposed inter-valley transfer mechanism could still be employed to explain these enhancement phenomena, affirming the validity of this proposed model. However, the specific enhancement factor, peak shift and line-shape change are different for the multilayer WS$_2$ on different substrates. This may be because the interfacial strain, lattice mismatch and charge transfer between the substrate and WS$_2$ are variable when different wafers are used as supporting substrates.[38-41]
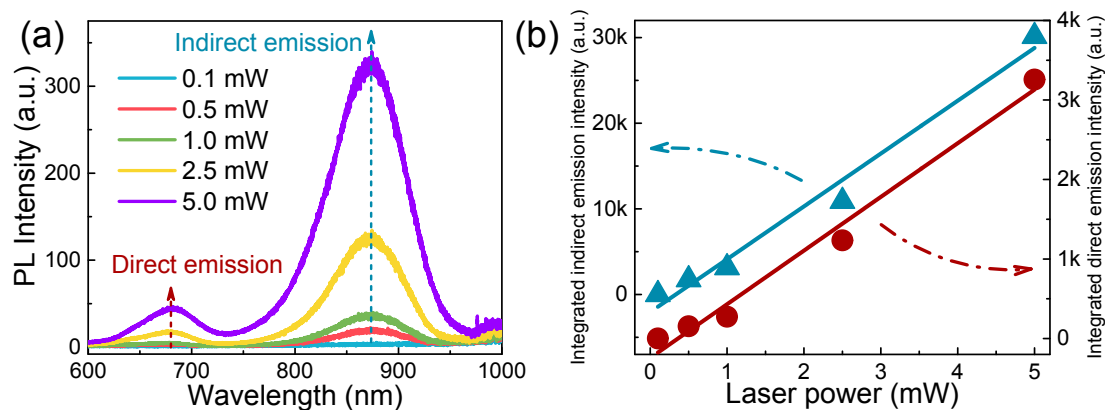
**Fig.S9** (a) Power-dependent PL spectra of the multilayer $WS_2$ sample. (b) Integrated PL intensity of the direct and indirect emission as a function of the incident laser power.

To study the influence of laser power density on the fluorescence emission of multilayer $WS_2$, power-dependent PL spectra are measured at room temperature by tuning the laser output power from 0.1 to 5 mW, as shown in **Fig.S9** above. Obviously, the entire PL intensity increases with the incident power (see **Fig.S9** (a)), which could be attributed to the generation and recombination of more photocarriers at elevated excitation power. It is noted that the integrated intensity of both peaks (direct emission and indirect emission) shows a similar near-linear increase rate as the laser power rises (see **Fig.S9** (b)). Such a power-dependent PL behavior is totally different from the temperature-dependent one (see Fig. 2(b) in the manuscript), in which the direct emission exhibits a rapider increase rate than the indirect one. This observation reveals that the fixed laser power (1 mW) itself cannot induce the observed significant PL enhancement. In addition, no notable peak redshift occurs and no new peaks related with defects appear when the laser power increases, indicating the laser power employed here does not cause a serious local heating effect and the sample is not apparently damaged. The observed fluorescence emission enhancement of multilayer $WS_2$ is mainly caused by the inter-valley carrier transfer mechanism, instead of the laser effect.

# Reference:

1.      D. Li, R. Cheng, H. Zhou, C. Wang, A. Yin, Y. Chen, N. O. Weiss, Y. Huang and X. Duan, *Nat Commun*, 2015, **6**, 7509.

2.      S. M. Sze and K. K. Ng, *Physics of Semiconductor Devices*, Clarendon Press, 1979.

3.      Y. Li, H. Xu, W. Liu, G. Yang, J. Shi, Z. Liu, X. Liu, Z. Wang, Q. Tang and Y. Liu, *Small*, 2017, **13**, 1700157.

4.      W. Zhao, Z. Ghorannevis, L. Chu, M. Toh, C. Kloc, P. H. Tan and G. Eda, *Acs Nano*, 2013, **7**, 791-797.

5.      T. Finteis, M. Hengsberger, T. Straub, K. Fauth, R. Claessen, P. Auer, P. Steiner, S. Uuml, fner and P. Blaha, *Physical Review B*, 1997, **55**, 10400-10411.

6.      H. Shi, H. Pan, Y.-W. Zhang and B. I. Yakobson, *Physical Review B*, 2013, **87**.

7.      A. Berkdemir, H. R. Gutiérrez, A. R. Botello-Méndez, N. Perea-López, A. L. Elías, C.-I. Chia, B. Wang, V. H. Crespi, F. López-Urías, J.-C. Charlier, H. Terrones and M. Terrones, *Scientific Reports*, 2013, **3**, 1755.

8.      S. Das Sarma, R. Jalabert and S. R. E. Yang, *Physical Review B*, 1989, **39**, 5516-5519.

9.      F. Giustino, S. G. Louie and M. L. Cohen, *Physical Review Letters*, 2010, **105**, 265501.

10.     Y. W. Tung and M. L. Cohen, *Physical Review*, 1969, **180**, 823-826.

11.     D. W. Latzke, W. Zhang, A. Suslu, T.-R. Chang, H. Lin, H.-T. Jeng, S. Tongay, J. Wu, A. Bansil and A. Lanzara, *Physical Review B*, 2015, **91**, 235202.

12.     K. Albe and A. Klein, *Physical Review B*, 2002, **66**, 073413.

13.     A. Kumar and P. K. Ahluwalia, *The European Physical Journal B*, 2012, **85**, 186.

14.     A. Ramasubramaniam, D. Naveh and E. Towe, *Physical Review B*, 2011, **84**, 205325.

15.     Z. Li, R. Ye, R. Feng, Y. Kang, X. Zhu, J. M. Tour and Z. Fang, *Advanced Materials*, 2015, **27**, 5235-5240.

16.     S. Tongay, J. Zhou, C. Ataca, K. Lo, T. S. Matthews, J. Li, J. C. Grossman and J. Wu, *Nano Lett*, 2012, **12**, 5576-5580.

17.     X. Xu, W. Yao, D. Xiao and T. F. Heinz, *Nature Physics*, 2014, **10**, 1-2.

18.     T. Cao, G. Wang, W. Han, H. Ye, C. Zhu, J. Shi, Q. Niu, P. Tan, E. Wang, B. Liu and J. Feng, *Nat Commun*, 2012, **3**, 887.

19.     G. Kresse and J. Furthmüller, *Phys Rev B Condens Matter*, 1996, **54**, 11169-11186.

20.     S. Grimme, *Journal of Computational Chemistry*, 2004, **25**, 1463.

21.     J. P. Perdew, K. Burke and M. Ernzerhof, *Generalized Gradient Approximation Made Simple*, 1996.

22.     B. PE, *Phys Rev B Condens Matter*, 1994, **50**, 17953-17979.

23.     W. Zhao, R. M. Ribeiro, M. Toh, A. Carvalho, C. Kloc, A. H. Castro Neto and G. Eda, *Nano Lett*, 2013, **13**, 5627-5634.

24.     S. L. Li, K. Wakabayashi, Y. Xu, S. Nakaharai, K. Komatsu, W. W. Li, Y. F. Lin, A. Aparecido-Ferreira and K. Tsukagoshi, *Nano Lett*, 2013, **13**, 3546-3552.

25.     L. Britnell, R. M. Ribeiro, A. Eckmann, R. Jalil, B. D. Belle, A. Mishchenko, Y.-J. Kim, R. V. Gorbachev, T. Georgiou, S. V. Morozov, A. N. Grigorenko, A. K. Geim, C. Casiraghi, A. H. C. Neto and K. S. Novoselov, *Science*, 2013, **340**, 1311-1314.

26.     A. Matthäus, A. Ennaoui, S. Fiechter, T. Kiesewetter, K. Diesner, M. Kunst, I. Sieber, W. Jaegermann and T. Tsirlana, 1997.

27. Q. H. Wang, K. Kalantar-Zadeh, A. Kis, J. N. Coleman and M. S. Stra  no, *Nat Nanotechnol*, 2012, **7**, 699-712.

28. Y. Ding, Y. Wang, J. Ni, L. Shi, S. Shi and W. Tang, *Physica B Physics of Condensed Matter*, 2011, **406**, 2254-2260.

29. J. A. Wilson and A. D. Yoffe, *Advances in Physics*, 1969, **18**, 193-335.

30. K. M. McCreary, A. T. Hanbicki, G. G. Jernigan, J. C. Culbertson and B. T. Jonker, *Sci Rep*, 2016, **6**, 19159.

31. A. H. Wang, X. L. Zhang, X. F. Zhang, X. Y. Qiao, H. G. Xu and C. S. Xie, *Materials Science and Engineering: A*, 2008, **475**, 312-318.

32. A. Kuc, N. Zibouche and T. Heine, *Physical Review B*, 2011, **83**, 245213.

33. A. B. Kaul, *Journal of Materials Research*, 2014, **29**, 348-361.

34. A. Berkdemir, H. R. Gutiérrez, A. R. Botello-Méndez, N. Perea-López, A. L. Elías, C.-I. Chia, B. Wang, V. H. Crespi, F. López-Urías, J.-C. Charlier, H. Terrones and M. Terrones, *Scientific Reports*, 2013, **3**, 1755.

35. F. Lópezurías, A. L. Elías, N. Perealópez, H. R. Gutiérrez, M. Terrones and H. Terrones, *2d Materials*, 2014, **2**.

36. M. Weng, S. Li, J. Zheng, F. Pan and L. W. Wang, *Journal of Physical Chemistry Letters*, 2018, **9**, 281.

37. J. Deng, Y. Lian, Z. Wu and Y. Xing, *Surface and Coatings Technology*, 2013, **222**, 135-143.

38. L. Su, Y. Yu, L. Cao and Y. Zhang, *Nano Research*, 2015, **8**, 2686-2697.

39. B. Amin, T. P. Kaloni and U. Schwingenschlogl, *Rsc Advances*, 2014, **4**, 34561-34565.

40. M. A. Lukowski, A. S. Daniel, C. R. English, F. Meng, A. Forticaux, R. J. Hamers and S. Jin, *Energy & Environmental Science*, 2014, **7**, 2608-2613.

41. A. Castellanosgomez, M. Buscema, R. Molenaar, V. Singh, L. Janssen, d. Z. Van, Herre S. J and G. A. Steele, *2d Materials*, 2014, **1**